Supporting Information

Intermetallic synergy between CeO_x-Co accelerates the selective production of *p*-xylene from PET waste on core-shell type cobalt phyllosilicates catalysts

Arjun K. Manal,[a] Rajendra Srivastava*[a]

[a]Catalysis Research Laboratory, Department of Chemistry, Indian Institute of Technology Ropar, Rupnagar−140001, Punjab, India

S 1. Experimental Section

S.1.1. Materials and Methods

Polycarbonate (PC) (Sigma), and PET (Sigma), and municipal waste plastic sources such as CD disks, Safety goggles, PC sheets, PET bottles, and fabric were used as plastic waste sources. Methyl 4-methylbenzoate (98%, Sigma-Aldrich), Methyl 4-methylbenzyl alcohol (98%, Sigma), Methyl acetate (97%, Loba Chemie), were used as model compound for C-O bond cleavage. Tetraethyl orthosilicate (TEOS) (99.7 %, Sigma-Aldrich), $Co(NO_3)_2.6H_2O$ (99 %, Sigma-Aldrich), $Ce(NO_3)_3.6H_2O$ (99 %, Sigma-Aldrich), and $(NH_4)_2CO_3$ (99 % Merk) were used for catalyst preparation. Iso-propyl alcohol (99 % Merk), ethanol (99 % Merk), 1, 4 dioxane (99 % Merk), decane (98 % Spectrochem), and methanol (99 % Merk) were used as solvents.

Synthesis of supporting catalysts

S.1.1. Synthesis of $Ce_{25}Ce_3/SiO_2$

The required amounts of $Co(NO_3)_2 \cdot 6H_2O$ and $Ce(NO_3)_3 \cdot 6H_2O$ were dissolved in 10 mL of deionized water. Separately, 0.5 g of SiO_2 was dispersed in 10 mL of deionized water under stirring. The metal nitrate solution was then added dropwise to the SiO_2 dispersion, and the resulting mixture was stirred for 3 h at room temperature. The solvent was subsequently removed using a rotary evaporator, and the obtained solid was dried under vacuum at 70 °C. Finally, the dried sample was reduced under a 10% H_2/Ar atmosphere at 700 °C for 4 h in a tubular furnace.

S.1.2. Synthesis of CeO_2

4 g of $Ce(NO_3)_3 \cdot 6H_2O$ was dissolved in 30 mL of deionized water. Separately, 14.4 g of NaOH was dissolved in 20 mL of deionized water, and the resulting solution was added dropwise to the cerium nitrate solution under vigorous stirring. After 10 min of continuous stirring, the formed precipitate was transferred into a Teflon-lined stainless-steel autoclave and subjected to hydrothermal treatment at 110 °C for 24 h. The obtained solid was then filtered, thoroughly washed with deionized water until neutral pH, dried overnight at 80 °C, and finally calcined at 400 °C for 2 h.

S.1.3. Synthesis of Co/CeO_2

The required amount of $Co(NO_3)_2 \cdot 6H_2O$ was dissolved in 10 mL of DI water. Then, 0.5 g of the prepared CeO_2 was dispersed into the 10 mL of DI water. Cobalt solution was added dropwise into the CeO_2 solution. This solution was stirred for 3 h at room temperature, followed by solvent evaporation using a rotary evaporator. The resulting solid was dried at 70 °C under vacuum and then underwent treatment with 10% H_2/Ar at 700 °C in a tube furnace for 4 h, yielding the final product, Co/CeO_2.

S 2. Catalysts Characterization

The structural, compositional, and physicochemical features of the catalysts were investigated using a range of analytical techniques. X-ray diffraction (XRD) measurements were performed on a Rigaku MiniFlex diffractometer (Japan) employing Cu Kα radiation (λ = 0.154 nm, 40 kV, 40 mA) within a 2θ range of 5–80°. The elemental composition of the catalysts was quantified using inductively coupled plasma optical emission spectrometry (MP-AES 4200, Agilent Technologies). The total acidity of the samples was determined through temperature-programmed desorption of ammonia (NH_3-TPD) using a Quantachrome CHEMBET™ TPR/TPD analyzer. Before analysis, the catalysts were pretreated at 600 °C under a helium stream (10 °C min^{-1}) for 30 min, followed by NH_3 adsorption at 50 °C for 1 h. Desorption was then monitored from 50 to 800 °C at a heating rate of 10 °C min^{-1} using a thermal conductivity detector (TCD). The reduction characteristics of the catalysts were examined by H_2-temperature-programmed reduction (H_2-TPR). In a typical run, 50 mg of sample was pretreated under flowing He at 400 °C for 1 h, cooled to 50 °C, and then subjected to a 5% H_2/N_2 mixture while heating to 800 °C at 10 °C min^{-1}. Hydrogen adsorption–desorption behavior was evaluated by H_2-TPD analysis using a Quantachrome 126 TPRWin v3.52 system. Surface chemical composition and oxidation states were characterized using X-ray photoelectron spectroscopy (XPS, Thermo Fisher Scientific Nexsa Base) equipped with an Al Kα X-ray source (1486.7 eV), operated at a pass energy of 23.5 eV and a take-off angle of 45°. The surface morphology and microstructural features of the synthesized catalysts were examined using a Field Emission Scanning Electron Microscope (FESEM, JSM-7610F, JEOL, Japan). Before imaging, the samples were coated with a thin conductive gold layer to minimize charging effects. The morphology, particle dispersion, and lattice fringes were examined via high-resolution transmission electron microscopy (HRTEM) on an FEI Tecnai G2 F30 instrument. For this, samples were ultrasonically dispersed in ethanol and drop-cast onto holey carbon-coated copper grids. Fourier-transform infrared (FTIR) spectra were collected on a Thermo Scientific Nicolet iS50 spectrometer to identify surface functional

groups and acidic sites. Additionally, diffuse reflectance infrared Fourier-transform spectroscopy (DRIFTS) measurements using methyl acetate as a probe molecule were performed to probe ester C=O bond activation characteristics, supported by temperature-dependent desorption analysis. Electron paramagnetic resonance (EPR) measurements were carried out using a BRUKER BioSpin spectrometer (Model: EMXmicro A200-9.5/12/S/W, Germany) operating at the X-band frequency (9 GHz). The spectra were recorded at room temperature.

S3. Catalytic activity tests

The catalytic experiments were conducted in a 25 mL stainless-steel batch autoclave reactor. In a typical run, the reactor was charged with the catalyst (0.05 g), PET feedstock (0.10 g), and solvent (6 mL). After sealing, the reactor was purged with N_2 three times to remove residual air and then pressurized to 2.5 MPa with H_2 at room temperature. The reaction was carried out at 220 °C for 6 h under constant stirring at 600 rpm. Upon completion, the reactor was cooled to ambient temperature, and the solid fraction containing the catalyst and any unreacted PET was separated by centrifugation. The resulting liquid phase was diluted with ethyl acetate and transferred into a 20 mL vial for analysis. Quantification was performed using a GC analysis. Product confirmation was performed by GC–MS analysis (Shimadzu QP-2010 Ultra, Rtx-5Sil MS column, 30 m × 0.25 mm × 0.25 μm).

PET conversion was determined by using the equation:

$$\text{Conversion (\%)} = 100\% - \frac{\text{mass of residual PET } (g)}{\text{initial mass of PET } (g)} \times 100\% \quad \text{(S2)}$$

For calculation of aromatic liquid products:

$$\text{Yield} = \frac{moles\ of\ aromatic\ in\ the\ products\ (mol)}{moles\ of\ aromatic\ in\ feedstock\ (mol)} \times 100\%$$

The value of aromatic formation rate represents the moles of produced PX by converted PET per hour over different catalysts, which was calculated as follows:

$$Rate\ of\ formation_{PX} = \frac{moles\ of\ PX\ (mmol)}{metal\ content\ \ in\ catalyst\ (wt\%)\ \times\ reaction\ time\ (h)}$$

Or

$$Rate\ of\ formation_{PX} = \frac{moles\ of\ PX\ (mmol)}{mass\ of\ catalyst\ \times\ reaction\ time\ (h)}$$

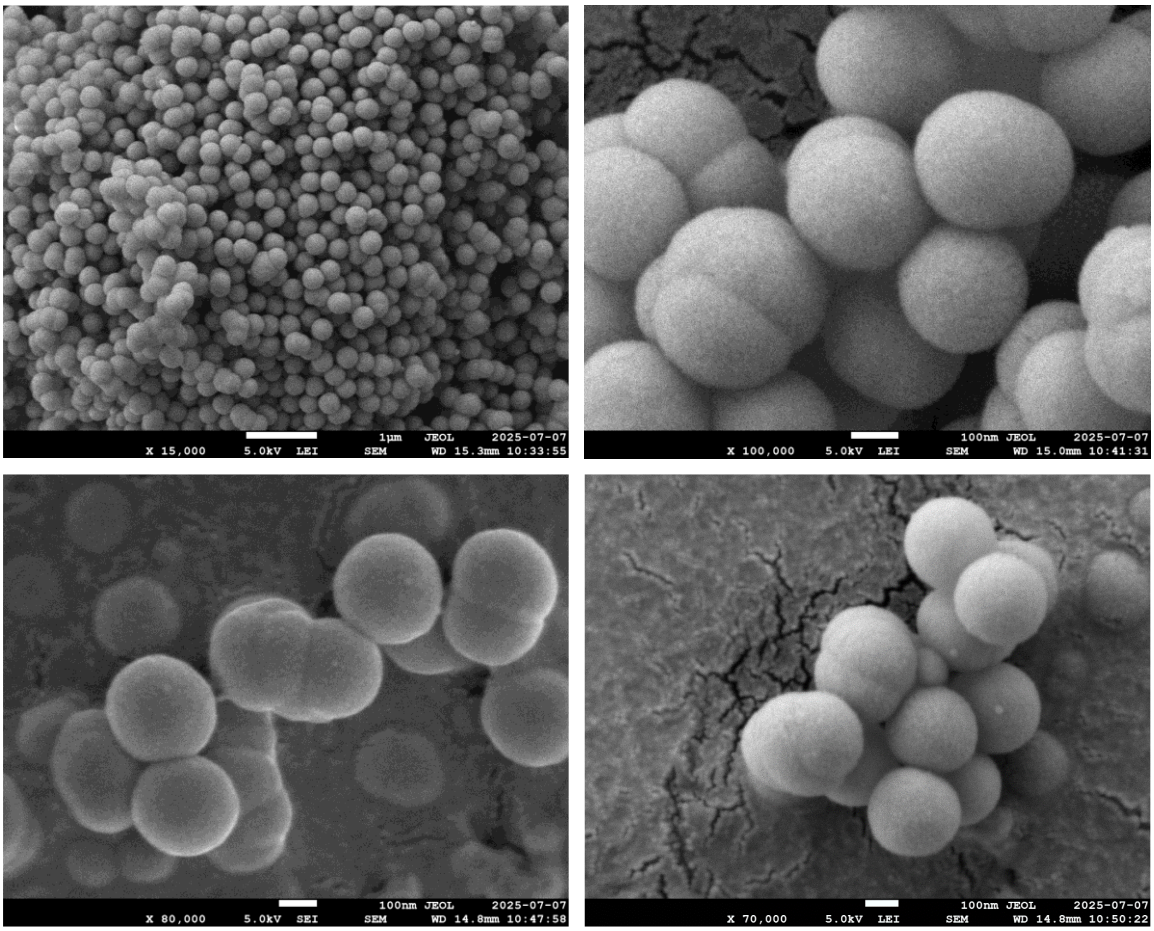

Fig. S1 FESEM Images of SiO_2 sphere

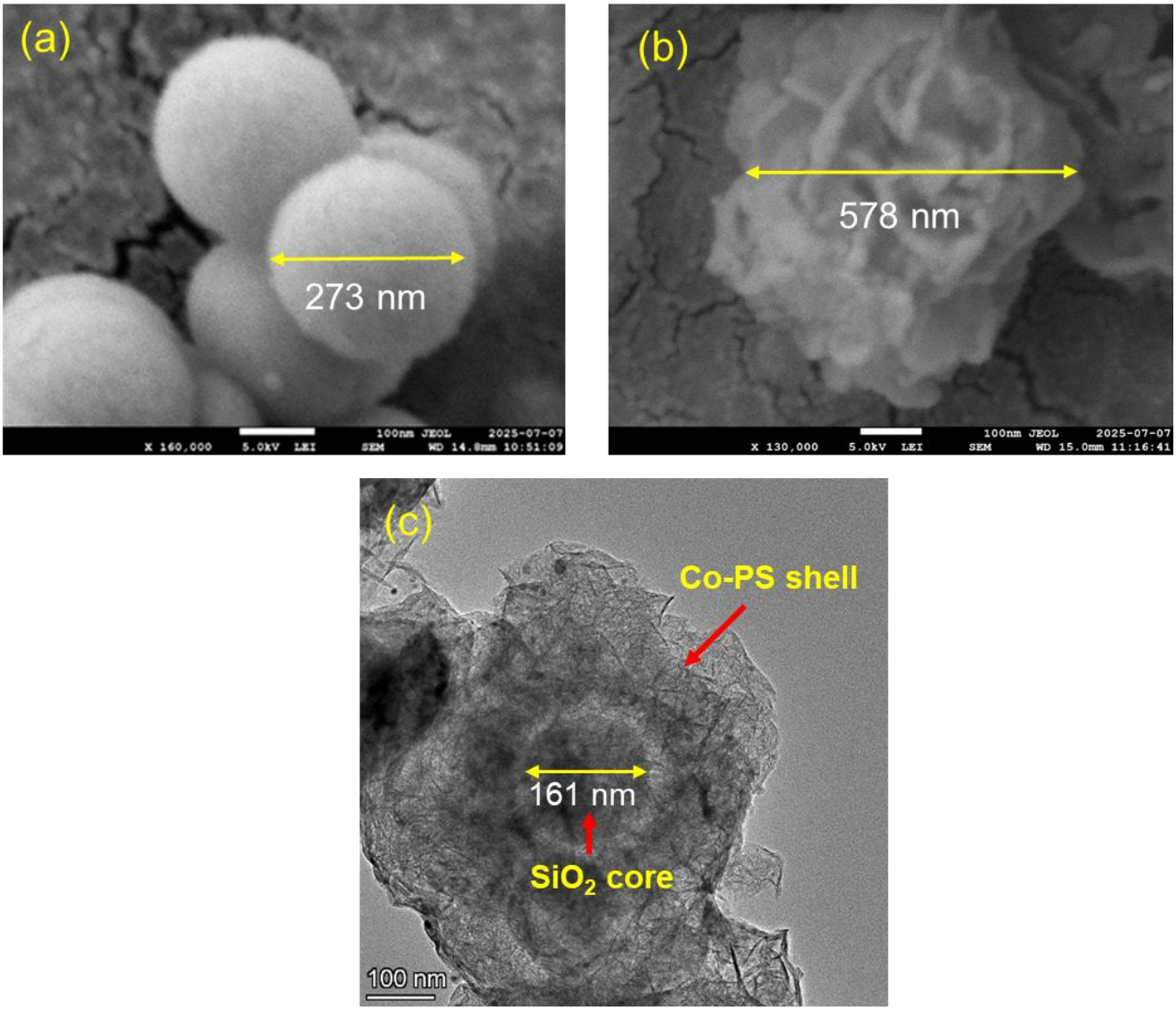

Fig. S2 FESEM Images of (a) SiO_2 sphere, (b) Co@Co-PS, and (c) TEM image of Co@Co-PS with calculated morphological size

The SEM image in Fig. S1a confirms the successful uniform SiO_2 spheres with an average diameter of ~273 nm. During the hydrothermal process, ammonium carbonate gradually etched the SiO_2 from the sphere to generate orthosilicic acid and $Co(OH)_2$ intermediates that reacted in situ to form a Co-PS with a flower-like morphology (Fig. S2b). In Fig. S2b, the resulting Co-phyllosilicate exhibits a sheet-like morphology with overall growth of ~578 nm, indicating coating of phyllosilicate layers around the SiO_2 sphere. The transformation from a spherical to a flower-like structure signifies the progressive deposition of Co–PS nanosheets on the etched SiO_2 surface, and formation of a core-shell structure. The TEM image in Fig. S1c further validates this core–shell architecture. The Fig. S2c clearly shows the SiO_2 sphere with reduction of sphere size (from ~270 nm to ~160 nm) indicate the partially etching of SiO_2

cores during the hydrothermal synthesis and the coating of phyllosilicate layers around the SiO_2 sphere.

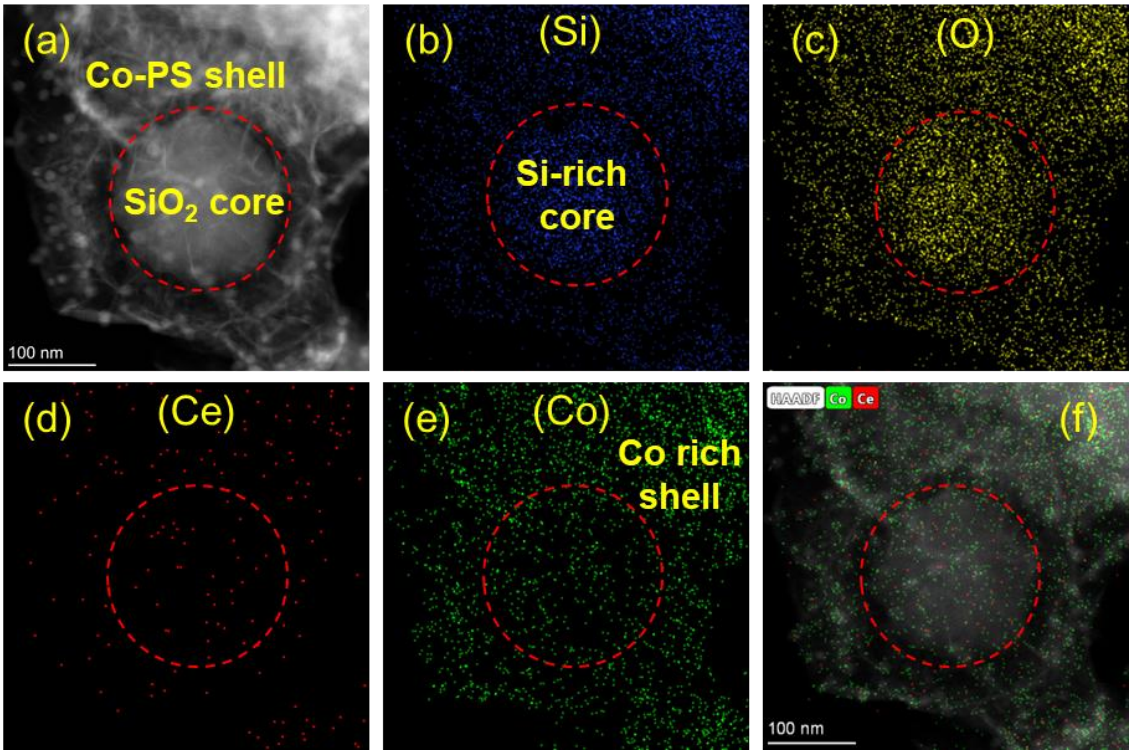

Fig. S3 HAADF-STEM and elemental mapping images of CeO_x Co-PS catalyst

The HAADF-STEM image (Fig.S3a) together with the corresponding EDX elemental maps (Fig. S3b–f) further provide strong evidence for the formation of a core–shell structured CeO_x modified Co-phyllosilicate catalyst. The Si and O elemental distributions (Fig. S3b and S3c) are highly concentrated within the central region (marked by the red dashed circle), confirming the presence of a silica-rich SiO_2 core. In contrast, Co and Ce signals (Fig. S3d and S3e) are predominantly observed in the outer region surrounding the SiO_2 core, which is characteristic of a phyllosilicate shell enriched with Co species and surface-decorated CeO_x domains. These results, consistent with morphological observations (FESEM and TEM), confirm that the synthesis route enables a well-defined core–shell structured phyllosilicate material.

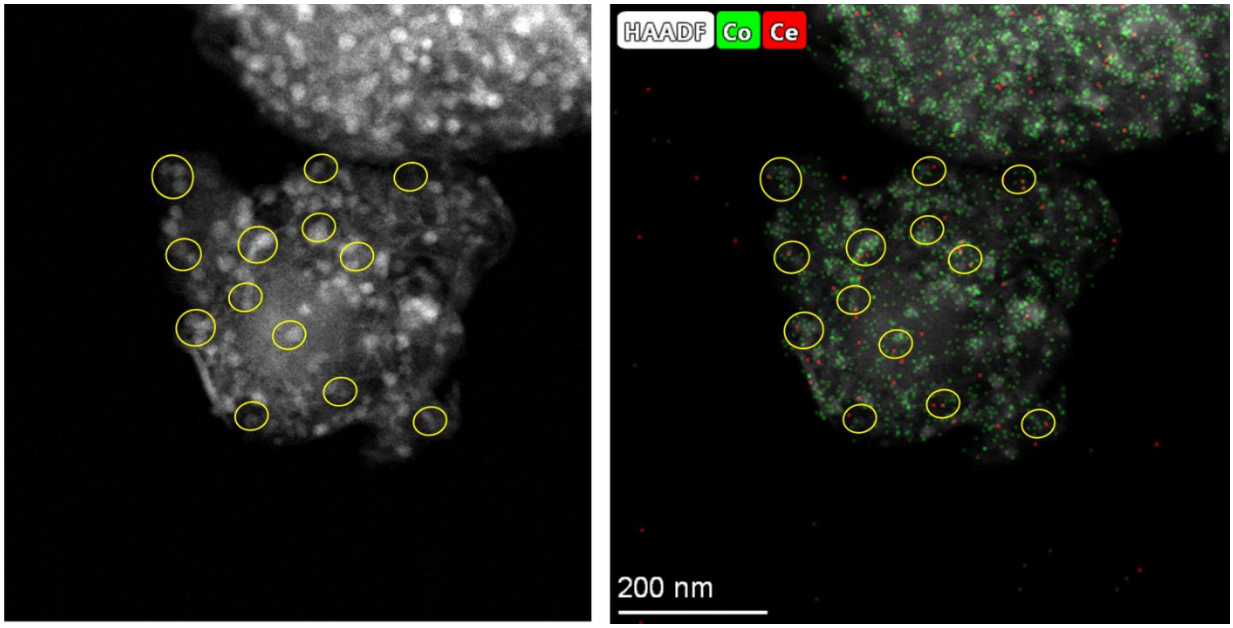

Fig.S4 HDDAF-STEM image and EDX elemental mapping of $Ce_{3.0}Co$@Co-PS.

Aberration-corrected HAADF-STEM image of the catalyst clearly reveals the intimate spatial association between Ce and Co species, as evidenced by the bright elemental contrast and the enriched Ce domains located adjacent to the exsolved Co nanoparticles (Fig. S4). The emergence of these finely dispersed CeO_x matrix are found to be adjacent to exsolved Co NPs, provides strong evidence of metal–support restructuring under reductive conditions. Their uniform anchoring and partial embedding within the CeO_x surface indicate robust metal–oxide interfacial interactions. Such nanoscale coexistence of CeO_x domains with exsolved Co NPs is indicative of pronounced interfacial electronic coupling, which is expected to enhance charge transfer across the Co–CeO_x interface. This interfacial synergy not only stabilizes the metallic Co sites against agglomeration but also promotes their redox responsiveness, collectively contributing to improved catalytic activity.

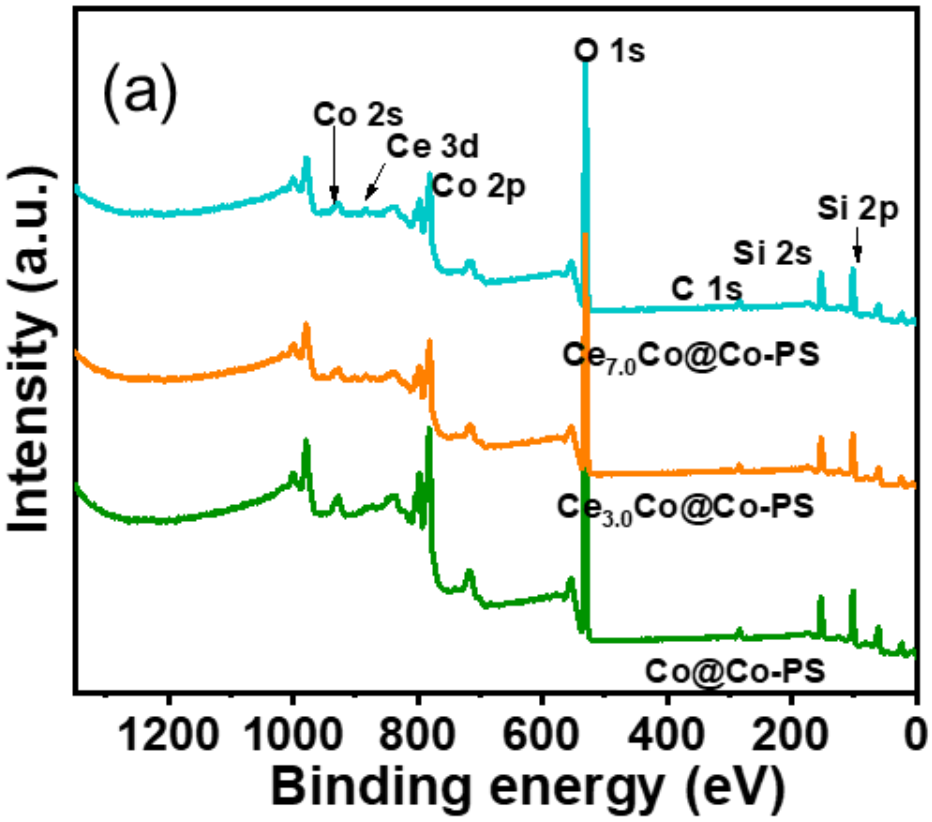

Fig. S5 XPS peak profile of the catalysts

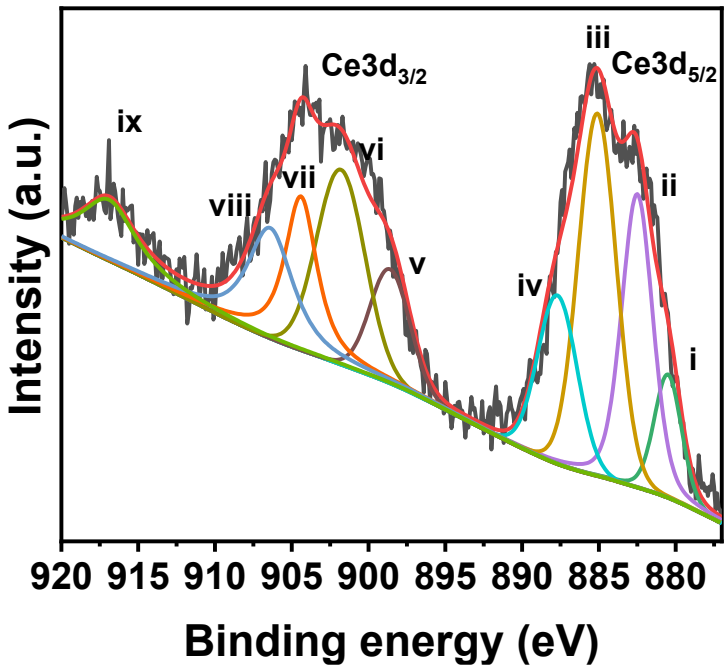

Fig. S6 High-resolution XPS profile of Ce 3d in $Ce_{3.0}Co$@Co–PS catalyst.

The high-resolution XPS spectrum of Ce 3d displays two broad envelopes, which can be assigned to the spin–orbit doublets of Ce $3d_{5/2}$ and Ce $3d_{3/2}$. The Ce $3d_{5/2}$ region exhibits multiple components located at approximately 880.5 eV (i), 882.4 eV (ii), 885.2 eV (iii), and 887.9 eV (iv), while the Ce $3d_{3/2}$ region shows corresponding features at 898.8 eV (v), 901.7 eV (vi), 904.5 eV (vii), and 906.5 eV (viii). Peaks labeled i, iii, v, and viii are characteristic of Ce^{3+} species, whereas the remaining signals (ii, iv, vi, and vii) are attributed to Ce^{4+} species. The pronounced intensity of the Ce^{3+} related peaks (iii and viii) indicates a significant proportion of Ce^{3+} on the catalyst surface. This coexistence of Ce^{3+} and Ce^{4+} demonstrates the presence of variable oxidation states and associated oxygen vacancies, which are known to enhance redox and catalytic performance. Quantitative analysis revealed that ~46% of the total cerium exists in the Ce^{3+} oxidation state in the $Ce_{3.0}Co$@Co–PS catalyst.

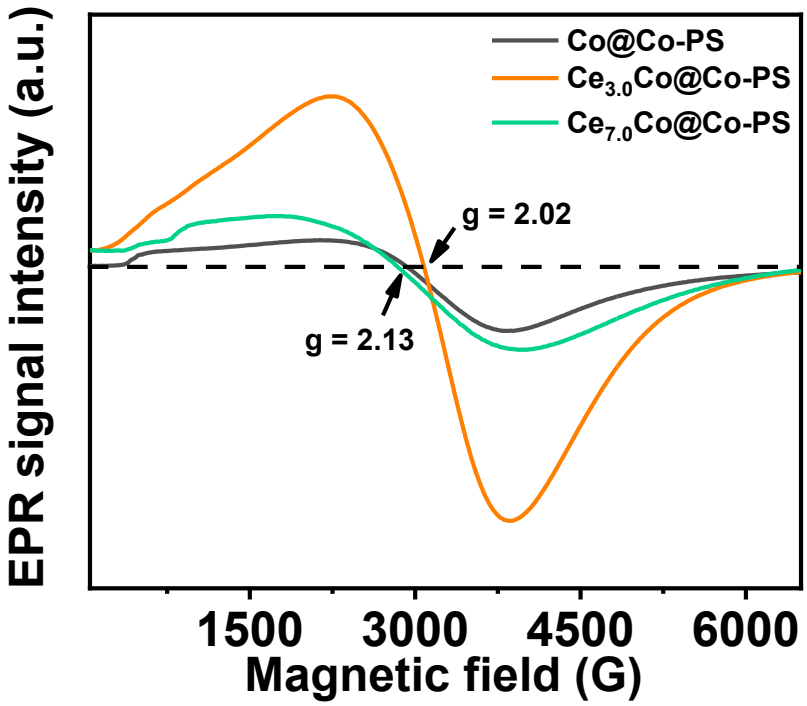

Fig. S7 EPR signal profile of catalysts

Fig. S7 depicts the EPR spectra of the Co-PS and CeO_x-modified Co-PS catalysts. All samples exhibit broad resonances between 3000–3600 G. The calculated g values for the EPR signal were found to be at 2.13 and 2.02. The signal at g ~ 2.13 is attributed to high-spin resolved CoO_x species in distorted oxygen coordination, while the g ~ 2.02 component corresponds to electron-trapped oxygen vacancies. Without Ce doping, the catalyst Co@Co-PS displays the weakest signal, indicating a low density of resolved CoO_x centres and oxygen defects. Upon Ce incorporation, the $Ce_{3.0}$Co@Co-PS catalyst exhibits a pronounced increase in intensity for both g-components, confirming the generation of abundant CoO_x defect sites and oxygen vacancies driven by Ce-induced lattice distortion.

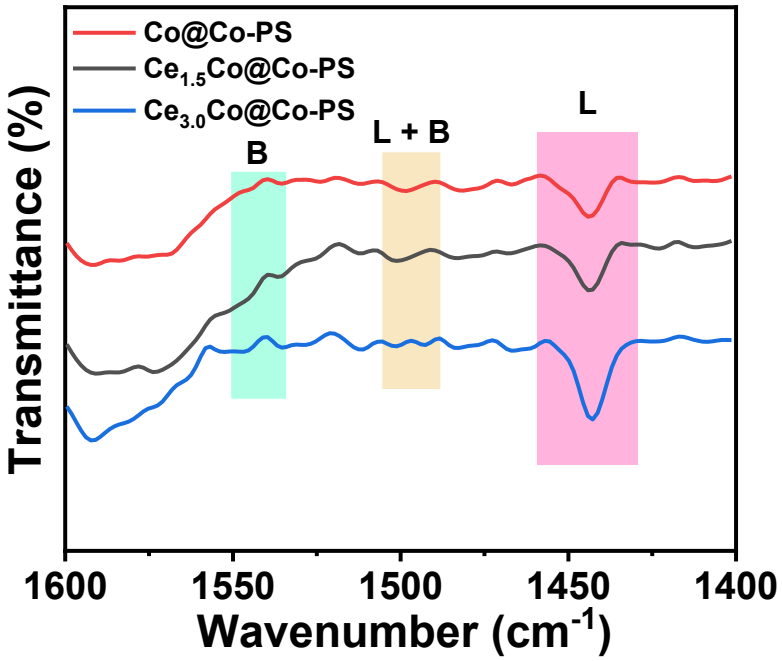

Fig. S8 Py-FTIR spectra of catalysts

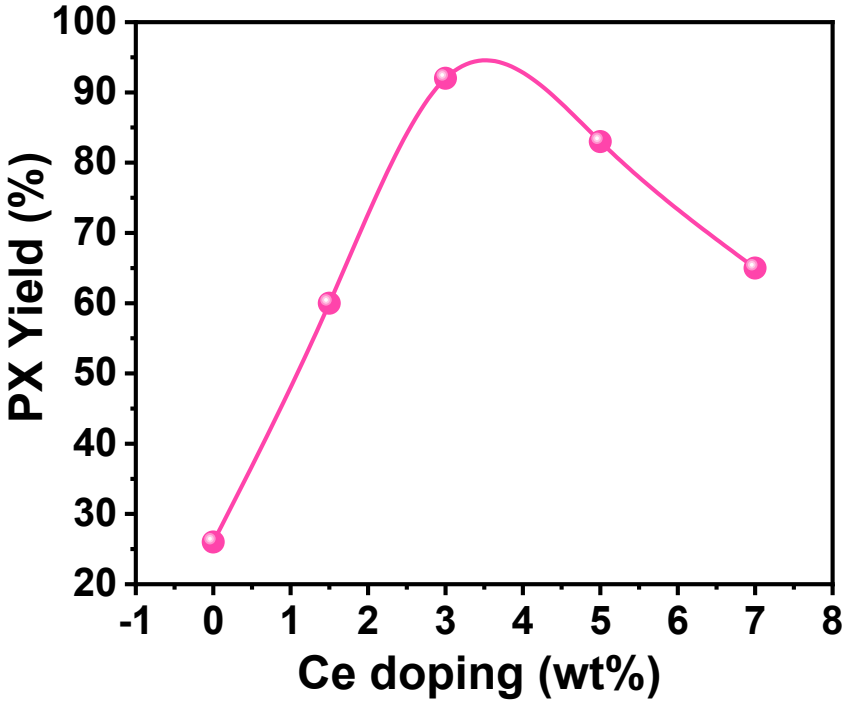

Fig. S9 Correlation of PX yield with Ce doping in CeOx-Co@Co-PS catalyst

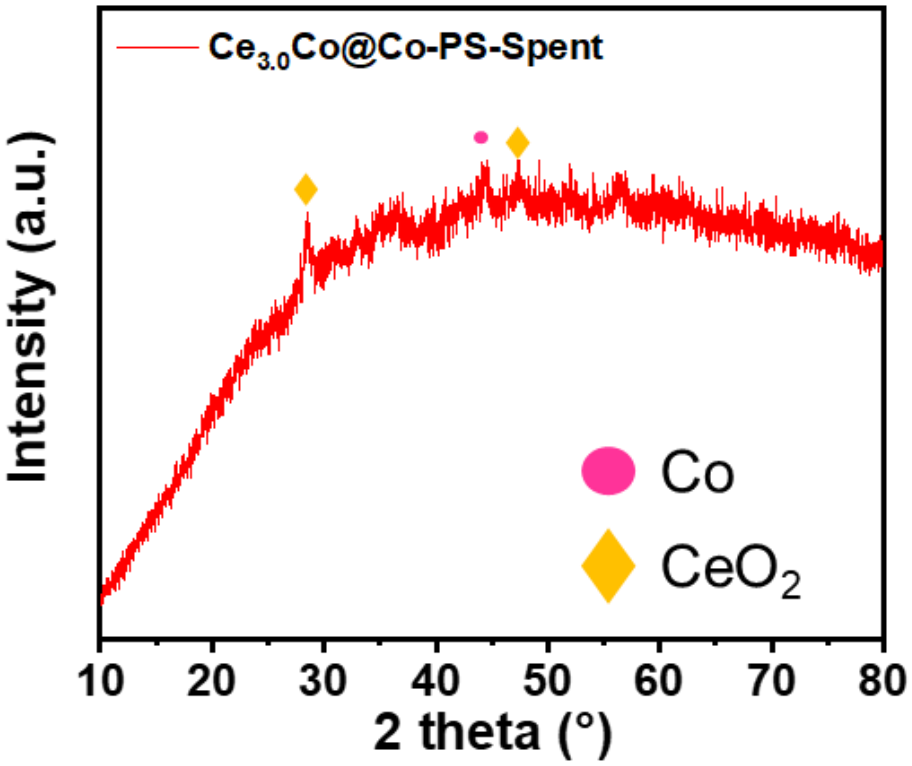

Fig. S10 PXRD pattern of the spent $Ce_{3.0}Co$@Co–PS catalyst.

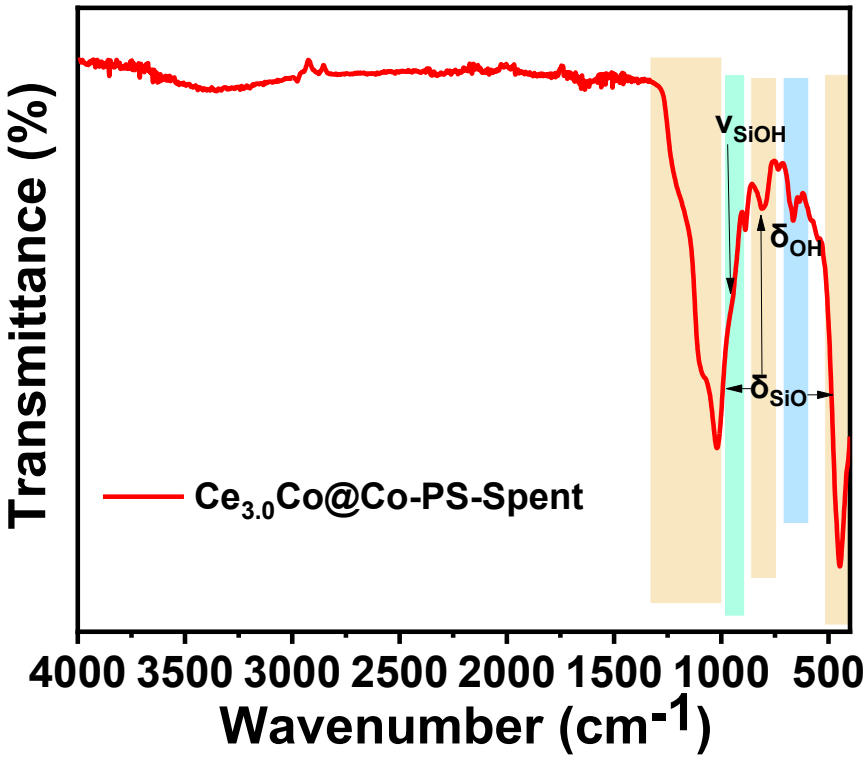

Fig. S11 FT-IR spectrum of spent $Ce_{3.0}Co$@Co–PS catalyst.

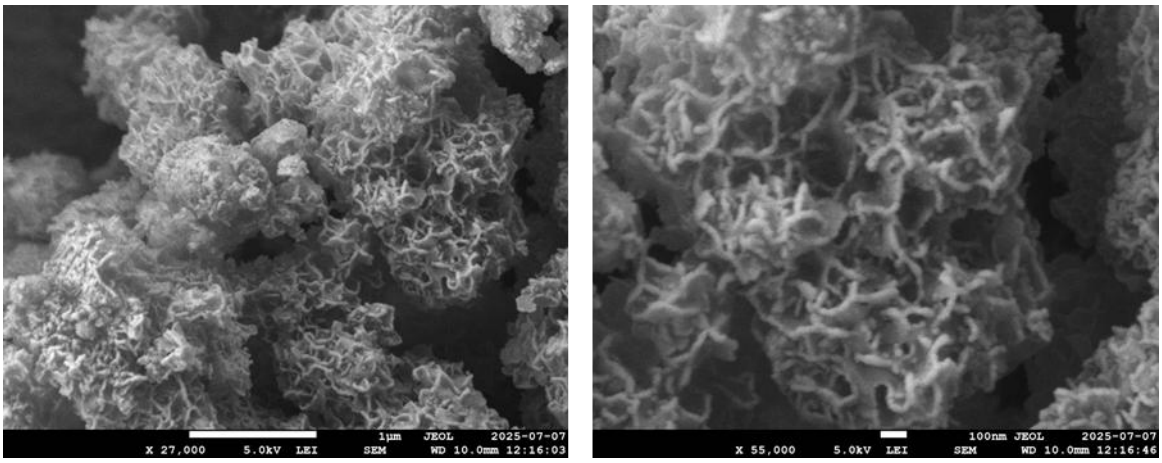

Fig. S12 FESEM images of the spent $Ce_{3.0}Co$@Co–PS catalyst.

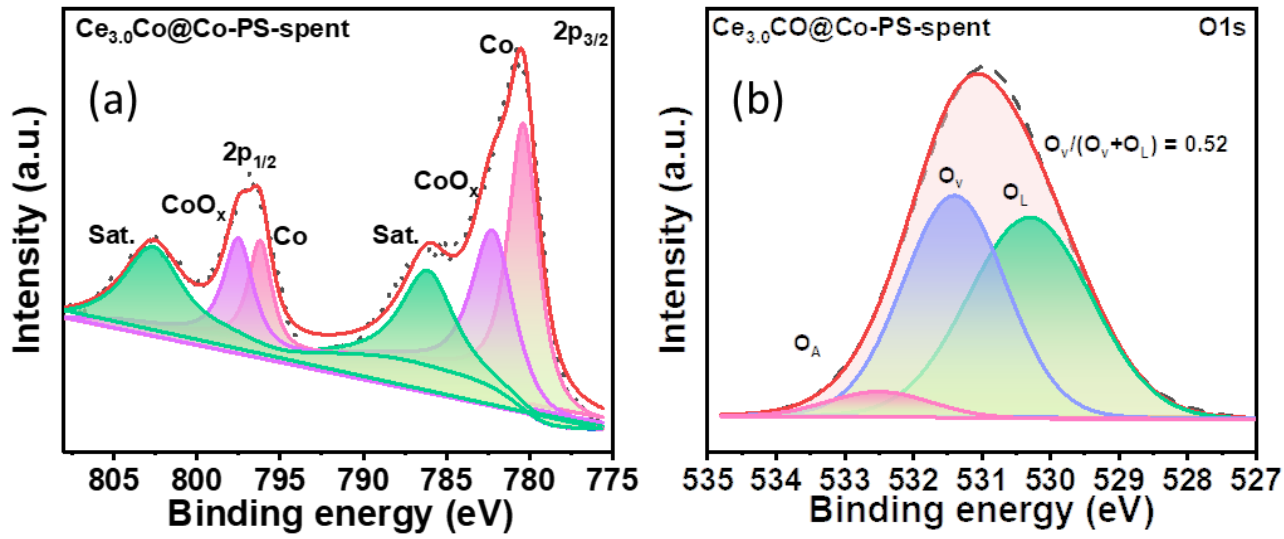

Fig. S13 XPS profile of the spent $Ce_{3.0}Co$@Co–PS catalyst.

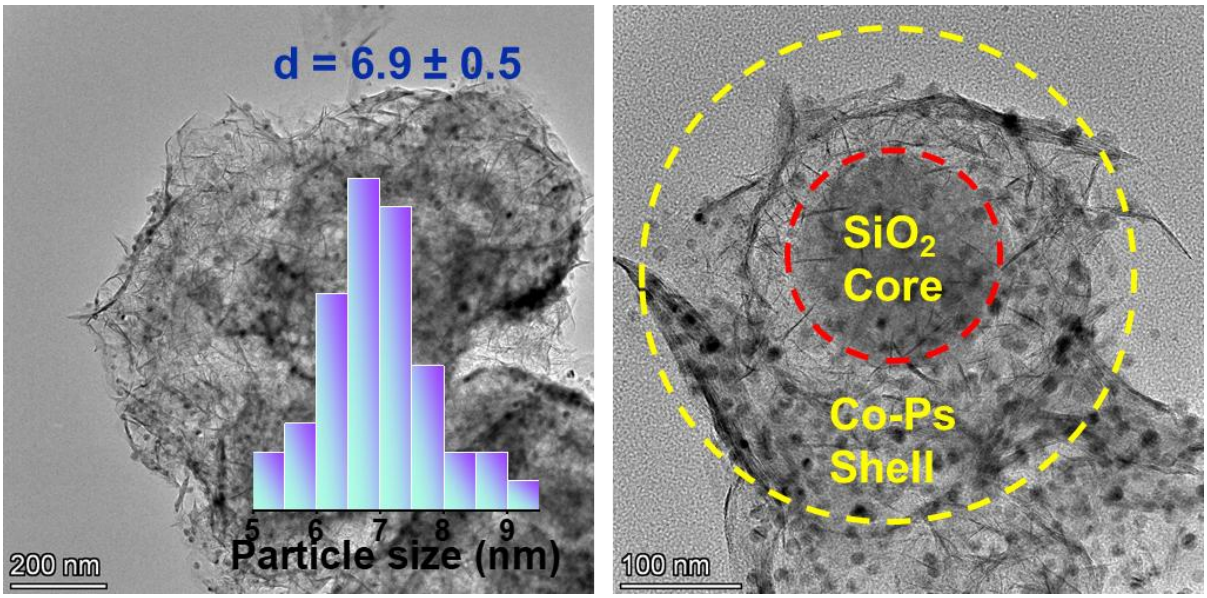

Fig. S14 TEM images of the spent $Ce_{3.0}Co$@Co–PS catalyst.

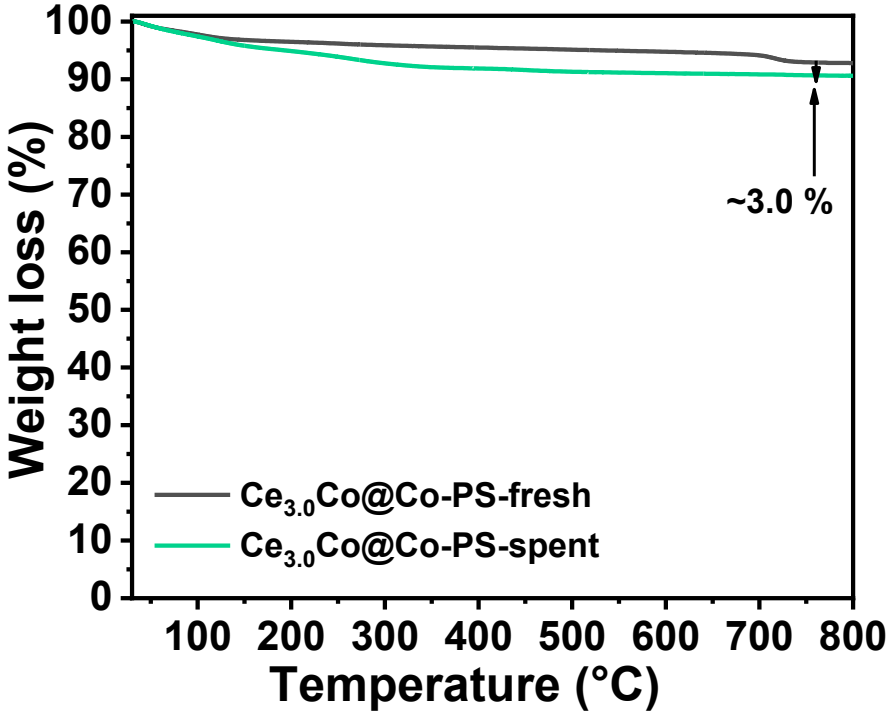

Fig. S15 TGA profiles of the fresh and spent $Ce_{3.0}Co$@Co–PS catalysts.

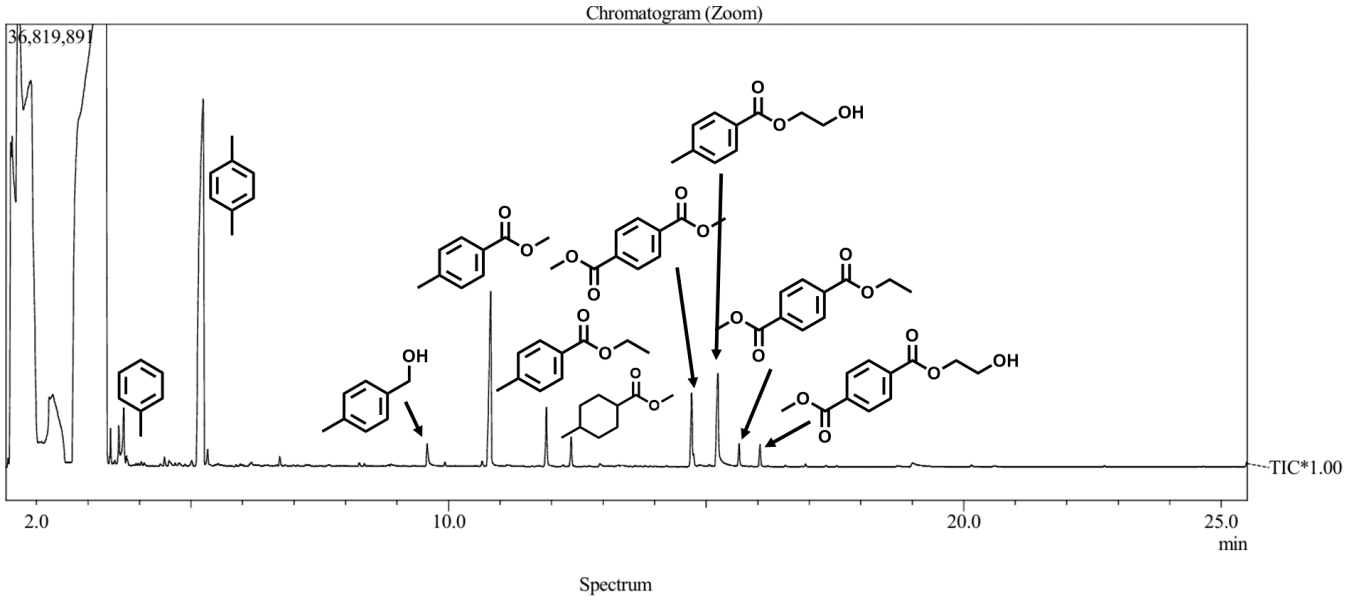

Fig. S16 GC-MS chromatogram of PET upcycling reaction and identification of intermediates and products.

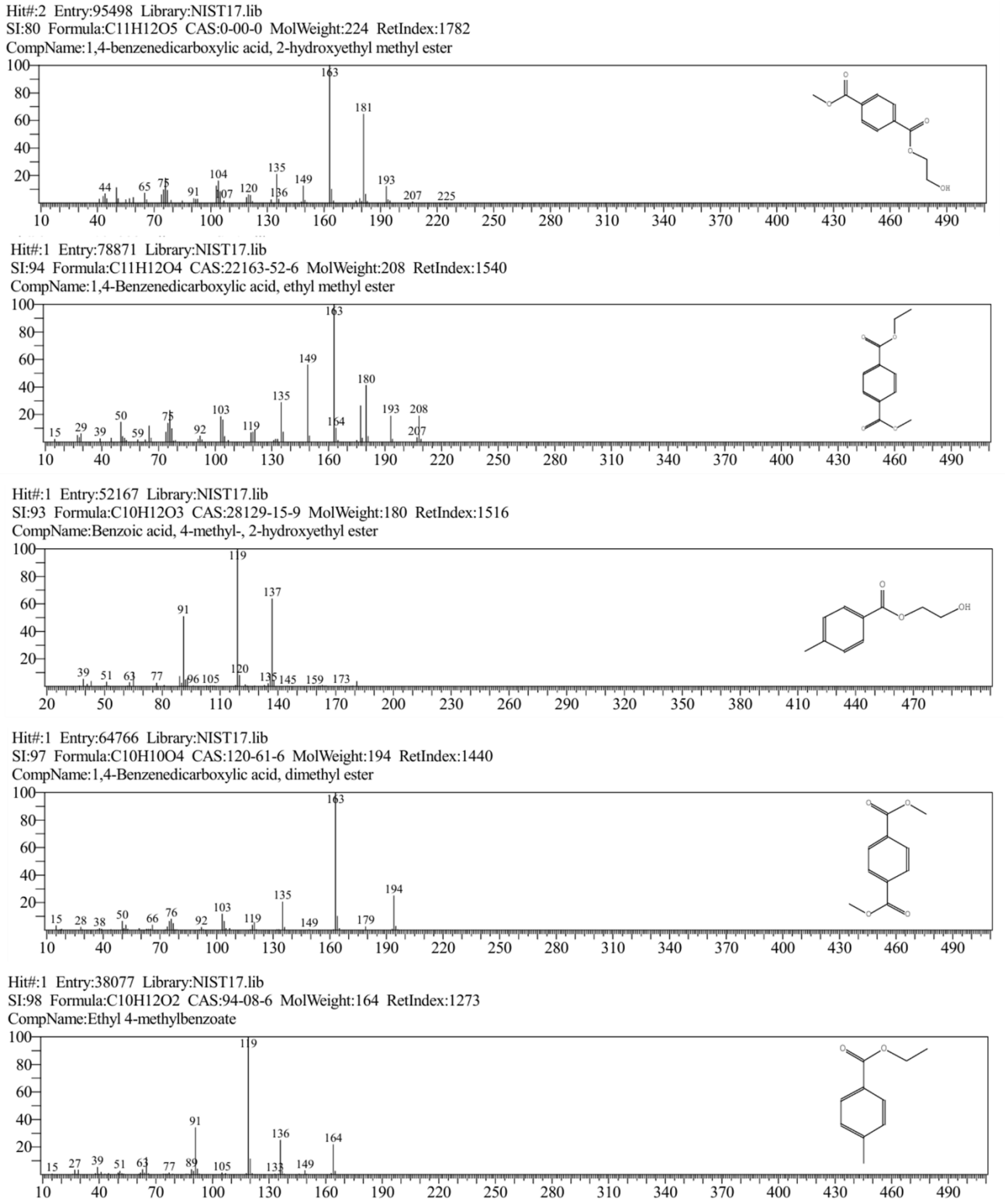

Fig. S17 Identification and confirmation of products structures by GC-MS analysis and similarity index.

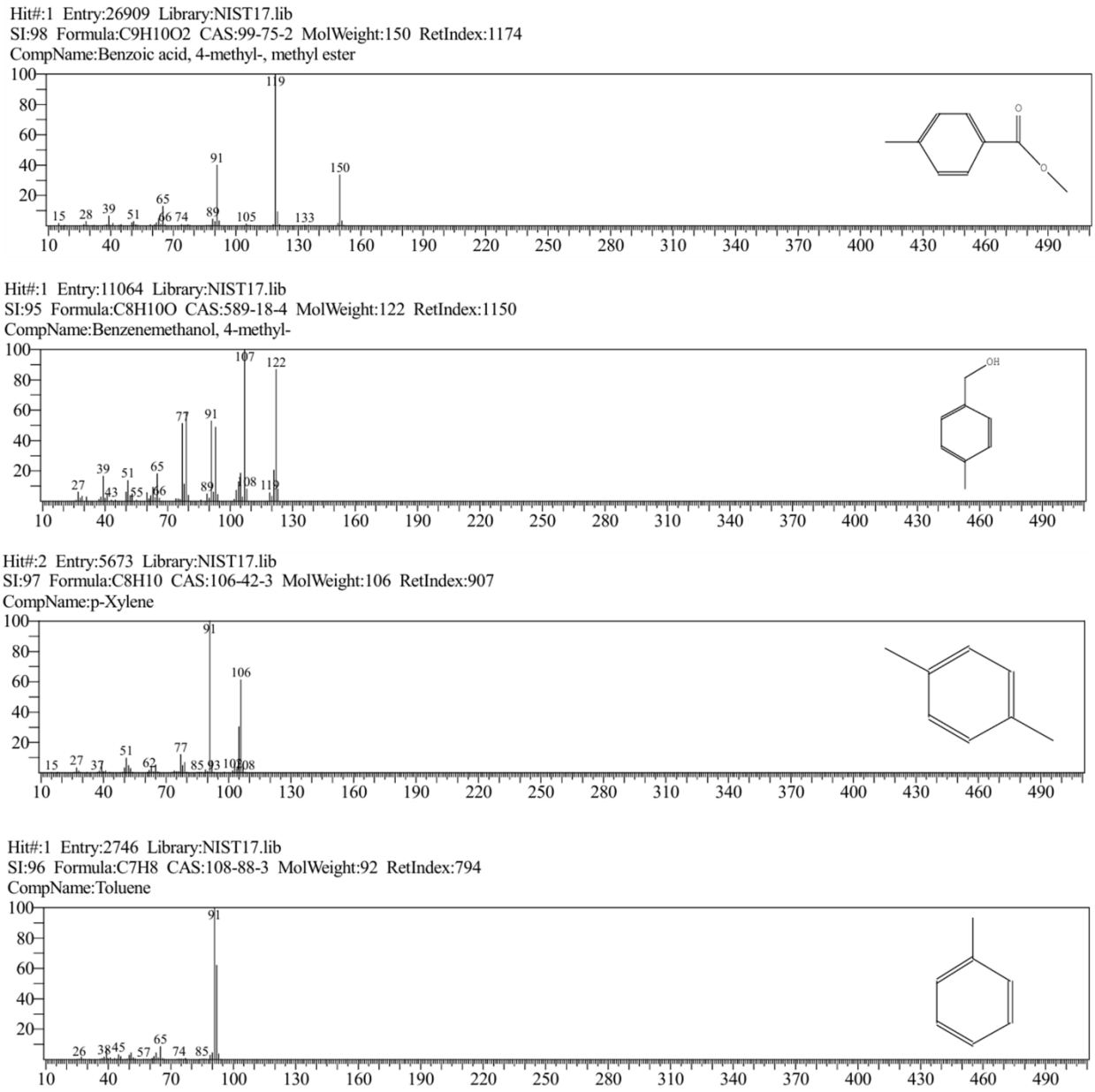

Fig. S18 Identification and confirmation of products structures by GC-MS analysis and similarity index.

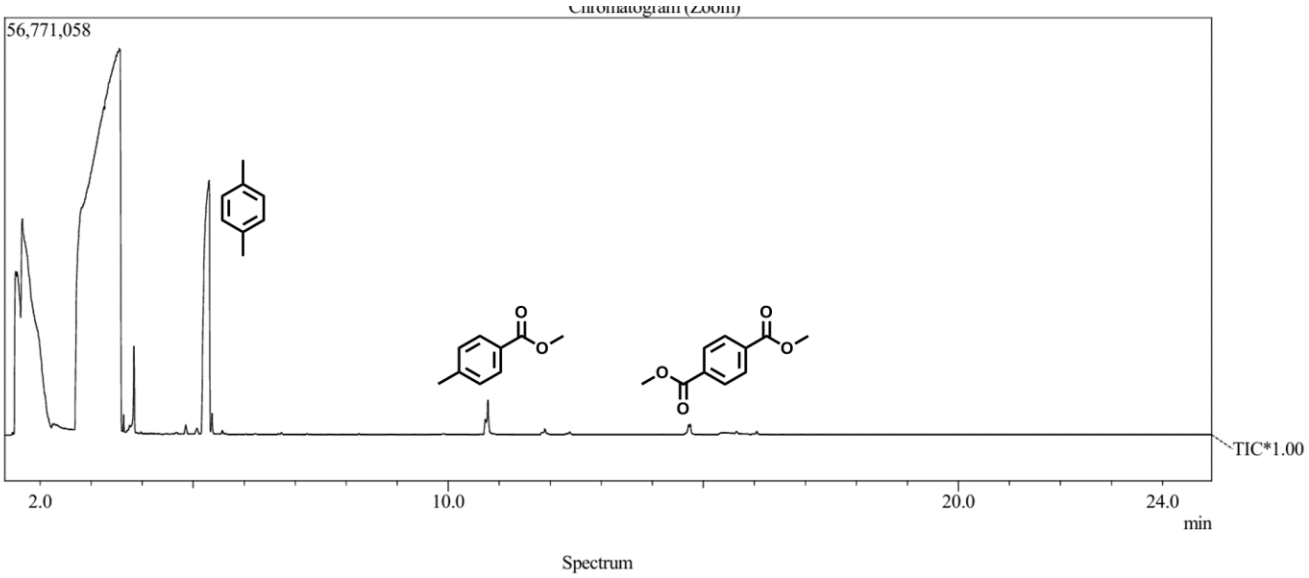

Fig. S19 GC-MS chromatogram of PET upcycling over $Ce_{3.0}Co$@Co-PS

Table S1. Characterization of Co species by XPS analysis

S. No	Catalysts	Co^0 (%)	CoO_x (%)
1.	Co@Co-PS	0.40	0.60
2.	$Ce_{3.0}$Co@Co-PS	0.55	0.45
3.	$Ce_{7.0}$Co@Co-PS	0.44	0.56

Table S2. Acidity calculation by NH_3 TPD analysis

S.No	Catalysts	Acidity (μmol/g)		
		1st desorption	2nd desorption	Total
1.	Co@Co-PS	176	36	212
2.	$Ce_{1.5}$Co@Co-PS	181	231	412
3.	$Ce_{3.0}$Co@Co-PS	195	531	726
4.	$Ce_{7.0}$Co@Co-PS	236	516	752

Table S3. Catalytic activity of $Ce_{3.0}Co$@Co-PS catalyst for PET upcycling in different solvents

S. No	Catalysts	Conversion (%)	PX yield (%)
1.	Dioxane	66.2	63
2.	Methanol	99.9	00
3.	Isopropanol	81.1	58
4.	Decane	7	00

Reaction Condition: 0.1 g PET, 0.05 g catalyst, solvent 6 mL, 2.5 MPa H2, 220 °C, 6 h.

Table S4.Catalytic performance of Ce modified catalysts

Entry	Ce doping (Wt. %)	Conv. (%)	PX yield (%)	Esters (%)
1	Co@Co-PS	89.4	26	46.2
2	$Ce_{1.5}$Co@Co-PS	96.9	60.2	26.4
3	$Ce_{3.0}$Co@Co-PS	100	92	3.4
4	$Ce_{5.0}$Co@Co-PS	100	83	5.2
5	$Ce_{7.0}$Co@Co-PS	89.1	65.8	19.6
6	CeO_2 + Co@Co-PS	97.3	32.9	41.2
7	3Ce/SiO_2 + Co@Co-PS	96.2	38.1	34.8
8	$Co_{25}Ce_3/SiO_2$	100	61.3	24.1
9	Co/CeO_2	100	8.4	53.8
10	Co/CeO_2 + Co@Co-PS	100	28.2	40.6

Reaction conditions: 0.1 g PET, 0.05 g catalyst, solvent 6 mL (15wt% methanol), 2.5 MPa H_2, 220 °C, 6 h.

Table S5. MP-AES data of fresh and spent Ce3.0Co@Co-PS catalyst.

Catalyst	Metal loading (%)	
	Co	Ce
$Ce_{3.0}$Co@Co-PS-fresh	24.1	3.1
$Ce_{3.0}$Co@Co-PS-spent	24.0	3.2

Table S6. H_2-desorption over different catalysts using H_2-TPD analysis.

Catalyst	**H_2 -desorption (μmol/g)**
Co@Co-PS	0.101
$Ce_{3.0}$Co@Co-PS	0.147
$Ce_{7.0}$Co@Co-PS	0.121
$Co_{25}Ce_3/SiO_2$	0.078

Table S7.Catalytic performance for hydrogenolysis of MMB over Co@Co-PS

Entry	Time (h)	Conv. (%)	MBA yield (%)	PX yield (%)
1	0.5	10.9	8.5	1.2
2	0.75	15.1	12.2	1.6
3	1	19.6	15.2	2.1
4	1.5	26.4	18.1	7.1
5	2	32.3	12.1	14.6
6	3	45.4	7	31.3
7	4	58.1	1.3	48.6
8	5	65.8	0	58.1
9	6	71.9	0	63.8
10	7	76.3	0	67.8

Table S8.Catalytic performance for hydrogenolysis of MMB over $Ce_{3.0}Co$@Co-PS

Entry	Time (h)	Conv. (%)	MBA yield (%)	PX yield (%)
1	0.5	19	16.6	3.2
2	0.75	27.8	22.5	5.1
3	1	34.3	25.8	8.1
4	1.5	47.7	14.6	28.3
5	2	59.1	7.2	50.3
6	3	82.1	0.8	78.1
7	4	94.8	0	90.3
8	5	100	0	96
9	6	100	0	95
10	7	100	0	93

Table S9.Catalytic performance for hydrogenolysis of MBA over Co@Co-PS

Entry	Time (h)	Conv. (%)	PX yield (%)
1	0.5	23.6	23
2	0.75	34.6	33.2
3	1	45.6	42.8
4	1.5	64.2	60.2
5	2	78.4	74.1
6	2.5	85.9	81.1
7	3	92.3	88.2
8	3.5	96	91
9	4	100	94
10	4.5	100	94

Table S10.Catalytic performance for hydrogenolysis of MBA over $Ce_{3.0}Co$@Co-PS

Entry	Time (h)	Conv. (%)	PX yield (%)
1	0.25	14.1	14
2	0.5	27.6	27
3	0.75	40.5	39.9
4	1	49.9	48.8
5	1.5	66.8	65.1
6	2	81.3	79.1
7	2.5	93	90.2
8	3	98	96.3
9	3.5	100	96.8
10	4	100	96.8

Table S11. Calculating the green chemistry metrics for the PET to PX process

Catalysts	Temp (°C)	Reaction time (min)	PX yield (%)	Solvent/PET mass ratio	Catalyst/PET mass ratio	ε	E	ξ	Ref
Cu2.0/Zn1.0-FeOx	200	480	98	66.66	1.333	0.0010	12.5683	12311.85	S1
Co–Fe–Al	210	600	98	66.66	1	0.0007	12.5067	16080.09	S2
$CuZn/Al_2O_3$	240	480	99	50	0.333	0.0008	9.20907	10716.01	S3
Cu4Fe1Cr1	240	2880	49.3	200	1	7.13E-05	73.8489	1035384	S4
$Cu/UiO\text{-}66\text{-}NH_2\text{-}A$	250	2160	89.5	0	2	0.0001	0.40476	2442.15	S5
Ru/Nb_2O_5	230	720	65	100	1	0.0003	28.1451	71705.1	S6
Ru/TiO_2	200	720	8	100	1	5.56E-05	228.679	411622	S7
Ce3.0Co@Co-PS	220	360	92	30	0.5	0.00116	6.00492	5169.45	This work

References

S1 Y. Shao, L. Kong, M. Fan, K. Sun, G. Gao, C. Li, L. Zhang, S. Zhang, Y. Wang and X. Hu, *ACS Sustain. Chem. Eng.*, 2024, **12**, 3818–3830.

S2 Y. Shao, M. Fan, K. Sun, G. Gao, C. Li, D. Li, Y. Jiang, L. Zhang, S. Zhang and X. Hu, *Green Chem.*, 2023, **25**, 10513–10529.

S3 M. Zhang, Z. Huo, L. Li, Y. Ji, T. Ding, G. Hou, S. Song and W. Dai, *ChemSusChem*, 2025, **18**, e202402013

S4 Y. Li, M. Wang, X. Liu, C. Hu, D. Xiao and D. Ma, *Angew. Chemie*, 2022, 61, e202117205.

S5 Q. Zou, T. Long, R. Fang, X. Zhao, F. Wang and Y. Li, *Angew. Chemie Int. Ed.*, 2025, 24, e202507309.

S6. Y. Jing, Y. Wang, S. Furukawa, J. Xia, C. Sun, M. J. Hülsey, H. Wang, Y. Guo, X. Liu and N. Yan, *Angew. Chemie Int. Ed.*, 2021, **60**, 5527–5535.

S7. M. Ye, Y. Li, Z. Yang, C. Yao, W. Sun, X. Zhang, W. Chen, G. Qian, X. Duan, Y. Cao, L. Li, X. Zhou and J. Zhang, *Angew. Chemie Int. Ed.*, 2023, **62**, e202301024.